PAPER

Bandgap and wave propagation of spring–mass–truss elastic metamaterial with a scissor-like structure

IOP Publishing Journal of Physics D: Applied Physics
J. Phys. D: Appl. Phys. **55** (2022) 055303 (16pp) https://doi.org/10.1088/1361-6463/ac2fd7

Bandgap and wave propagation of spring–mass–truss elastic metamaterial with a scissor-like structure

Yingli Li[1,2,4,*], **Hao Li**[1,3], **Xiang Liu**[1] and **Shiguang Yan**[1]

[1] Key Laboratory of Traffic Safety on Track (Central South University), Ministry of Education, School of Traffic and Transportation Engineering, Central South University, Changsha 410075, People's Republic of China
[2] Joint International Research Laboratory of Key Technology for Rail Traffic Safety, Central South University, Changsha, People's Republic of China
[3] National & Local Joint Engineering Research Center of Safety Technology for Rail Vehicle, Central South University, Changsha, People's Republic of China
[4] State Key Laboratory of High Performance Complex Manufacturing, Central South University, Changsha, People's Republic of China

E-mail: liyingli@csu.edu.cn

Received 18 May 2021, revised 4 October 2021
Accepted for publication 14 October 2021
Published 28 October 2021

Abstract

Inspired by the inertial amplification mechanism and bandgap characteristic of periodic structures, a type of scissor-like elastic metamaterial is studied for low-frequency vibration attenuation in this paper. Firstly, the 1DOF (degree of freedom) scissor-like chain consisting of masses, trusses, and springs is investigated. The formation of inertial amplification is illustrated, that is, input horizontal movements are converted into larger vertical movements of vertex masses by a scissor-like structure. The resonance and anti-resonance phenomena in transmission curves are explained. Especially, the optimal configuration for low-frequency attenuation is obtained by analytical expressions of the dispersion relation. Then, a 2DOF spring–mass–truss chain is considered to open a bandgap below the vibration attenuation range of the 1DOF chain. The relative movement of masses at different frequencies is explored to understand the bandgap generation. The influence of parameters including the mass ratio, tensile stiffness ratio, shear stiffness ratio, and angle on bandgap boundaries is discussed. Finally, the spatial propagation of a wavelet packet is presented to illustrate the efficiency of the proposed structure in terms of minimizing a broadband excitation transmission. The transmitted component of a wavelet packet through three units of the proposed structure is only 3.8%, which is 22.8% of that through the classic 1D local resonance metamaterial.

Keywords: vibration attenuation, scissor-like structure, low-frequency bandgap, inertial amplification

(Some figures may appear in colour only in the online journal)

1. Introduction

Developing systems to attenuate low-frequency structural vibrations, i.e. the vibration that can propagate long distances without mitigation, has applications to acoustic and elastic vibration suppression [1, 2], including railway vehicles [3, 4]and automobiles [5], among many others. In various industrial engineering, mechanical vibration is regarded as a negative issue that degenerates the equipment service life, working accuracy, and efficiency. In particular, low-frequency vibration control is a challenge due to its inherent relationship

* Author to whom any correspondence should be addressed.

with mass and stiffness, which is often achieved at the cost of increasing the mass or reducing the stiffness of a system.

The scissor-like structure is a kind of classical vibration isolation structure [6–8]. Jing *et al* applied a scissor-like vibration isolation platform to the vehicle seat suspension, which has better vibration attenuation capacity comparing with the quasi-zero-stiffness device [6]. In addition, they studied a novel X-shaped bio-inspired anti-vibration structure [7, 8], which was applied to an operating hand-held jackhammer. Wei *et al* developed a scissor-like energy harvesting system with equivalent nonlinear damping, which has better loading performance as four linear springs are assembled on two sides of the scissor-like structure [9]. These studies mainly focus on the vibration isolation of platforms composed of several layers of scissor-like structure, which is still limited by the mass and stiffness of a system.

The propagation regulation of elastic or acoustic waves in periodic metamaterial structures has attracted much attention [10, 11]. Unusual behaviors, such as negative material constants [12–14] can be obtained by elastic metamaterials. However, one of the main focus areas is to obtain bandgaps, which can block wave propagation at certain frequency ranges [15, 16]. Hence, some scissor-like structures are proposed as origami-based metamaterials, the geometrical configurations and mechanical properties of which are beneficial for designing the devices subjected to vibration or impact [17–19]. For example, Yasuda *et al* investigated a rigid folding origami metamaterial chain, which exhibits the intrinsic tunability of its behavior of vibration attenuation by altering excitation and geometrical parameters [17]. Xu *et al* studied the coupling characteristics in origami metamaterials to tune and rich bandgap regulation [19]. To obtain low bandgaps by metamaterials including origami metamaterials, one needs large-sized structures, heavy resonators, or low stiffness, but these conditions are not conducive to practical purposes.

Recently, inertial amplification was introduced to the elastic metamaterials [20–22]. With the inertial amplification mechanism [23, 24], large effective inertia can be achieved for low-frequency bandgaps by a small mass. Yilmaz *et al* proved the effect of inertial amplification on possessing low bandgap via 2D periodic lattice [20, 23]. Frandsen *et al* attached the inertial amplification elements to a host structure to obtain wide low bandgaps with as much as 20 times less mass compared to a classical local resonator bandgap [22]. Meanwhile, scissor-like structures composed of trusses and springs are also the basic element of the inertia amplification structure. Bennetts *et al* compared the bandgap of three types of cross-link structures induced by inertial amplification [24]. Yuksel *et al* achieved an ultrawide stop band in 2D elastic metamaterial with topologically optimized inertial amplification mechanisms by the finite element method [21]. Many of these studies are carried out based on discrete mass models, which allow analytical derivation and facilitate the analysis of the bandgap generation [25–27].

Overall, the bandgap of periodic metamaterials may expand the vibration attenuation frequency range of the classical scissor-like vibration isolation platforms, and the inertial amplification mechanism can extend the bandgap to ultra-low-frequency. Therefore, we attempt to attach additional masses to the joint of a scissor-like structure and assemble it periodically to seek a low-frequency vibration attenuation range.

In this paper, the elastic wave bandgap and vibration propagation property of a type of scissor-like periodic metamaterial consisting of masses, massless trusses, and springs are studied. Firstly, the 1DOF spring–mass–truss (SMT) chain is proposed based on traditional scissor-like vibration isolation platforms. Then, a 2DOF SMT chain is obtained by changing adjacent parameters to generate a bandgap below the vibration attenuation range of the 1DOF chain. In both models, the analytical expressions of bandgap boundaries are obtained to tune structural parameters for lower and wider attenuation range. Considering the practical application potential, the vibration transmission is investigated to verify the bandgap obtained by Bloch's theorem. Meanwhile, the displacement amplitudes of masses at different frequencies are presented to understand the bandgap generation. Finally, the spatial propagation of a wavelet packet is analyzed to illustrate the broadband excitation attenuation performance of the proposed structure. This work may be of significance for the design of vibration attenuation in engineering.

2. 1DOF spring–mass–truss (SMT) chain

Scissor-like structures composed of massless rigid trusses and springs are used as vibration isolation platforms or elastic metamaterials extensively [20, 24, 28–30]. With regards to the bandgap of periodic metamaterial, the scissor-like structure is assembled periodically to seek further vibration attenuation in the bandgap range. Since both vibration attenuation and bandgap frequency depend on the mass and stiffness of the system, masses are attached to the connections of trusses, forming an inertia amplification element for low-frequency bandgaps. Therefore, the bandgap and vibration behavior of the periodic SMT metamaterial with scissor-like and inertia amplification structure is investigated.

2.1. Analytical model

The infinite periodic SMT metamaterial considered in figure 1 consists of two monoatomic chains. Each monatomic chain is composed of masses m and springs with tensile stiffness K and shear stiffness G. The adjacent masses of two monoatomic chains are attached to intersection masses M by four rigid and massless truss members that are symmetrically assembled like a scissor, where the trusses make an angle α with the horizontal direction. The massless rigid trusses and masses are hinged while the spring is fixed to adjacent vertex masses m. The jth unit cell is shown in the dashed box in figure 1.

Similar to the scissor-like energy harvesting system [9], the proposed structure with springs at the bottom and top in figure 1 is more stable than most existing scissor-like discrete

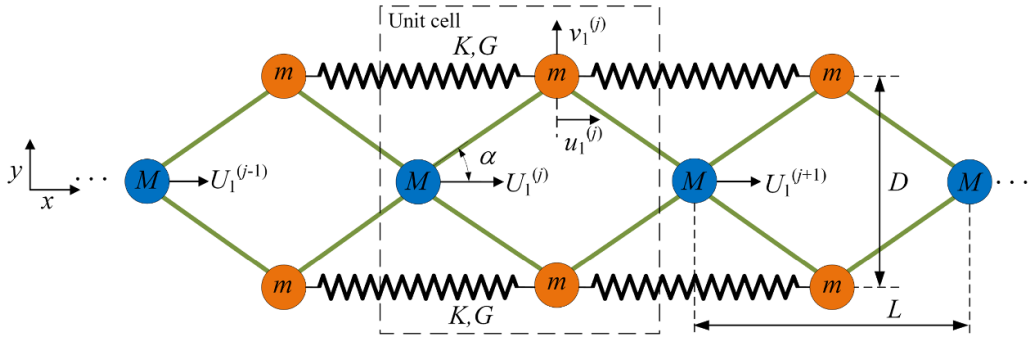

Figure 1. Infinite periodic 1DOF SMT chain, involving two monoatomic chains attached to intersection masses M by four rigid and massless trusses.

mass models with springs in the middle. Set the origin of y direction at masses M, and only the horizontal displacement along the x axis of M is considered. In contrast, vertex masses m can move along both the x and y axes. The distance of two adjacent unit cells is denoted as lattice constant L.

From geometrical relations based on the assumption of small displacements, we have

$$\begin{aligned} v_1{}^{(j)} &= \frac{1}{2}\sqrt{D^2 - 2\Delta UL - \Delta U^2} - \frac{D}{2} \\ &\approx -\frac{L}{2D}\Delta U - \frac{L^2+D^2}{2D^3}\Delta U^2 - \dots \\ &= -\frac{L}{2D}\left(U_1^{(j+1)} - U_1^{(j)}\right) \end{aligned} \tag{1}$$

where $\Delta U = U_1^{(j+1)} - U_1^{(j)}$.

Therefore, the linear relationship of displacements between the masses m and M is

$$\begin{cases} u_1^{(j)} = \dfrac{1}{2}\left(U_1^{(j)} + U_1^{(j+1)}\right) \\ v_1^{(j)} = \dfrac{1}{2}\gamma\left(U_1^{(j)} - U_1^{(j+1)}\right) \end{cases} \tag{2}$$

where $\gamma = \cot(\alpha) = L/D$ is a tunable geometrical parameter, and symbols $u_1^{(j)}$ and $v_1^{(j)}$ represent the horizontal and vertical displacements of mass m in the jth unit cell, respectively.

Based on Lagrange's Equation and equation (2), the equations of motion of the jth unit cell can be derived as

$$\begin{aligned} &M\frac{\mathrm{d}^2U_1^{(j)}}{\mathrm{d}t^2} + m\left(\frac{\mathrm{d}^2u_1^{(j)}}{\mathrm{d}t^2} + \frac{\mathrm{d}^2u_1^{(j-1)}}{\mathrm{d}t^2}\right) + m\left(\frac{\mathrm{d}^2v_1^{(j)}}{\mathrm{d}t^2} - \frac{\mathrm{d}^2v_1^{(j-1)}}{\mathrm{d}t^2}\right)\gamma \\ &+ K\left(2u_1^{(j)} - u_1^{(j+1)} - u_1^{(j-1)}\right) + K\left(2u_1^{(j-1)} - u_1^{(j)} - u_1^{(j-2)}\right) \\ &+ G\left(2v_1^{(j)} - v_1^{(j+1)} - v_1^{(j-1)}\right)\gamma - G\left(2v_1^{(j-1)} - v_1^{(j)} - v_1^{(j-2)}\right)\gamma \\ &= 0. \end{aligned} \tag{3}$$

According to Bloch's theorem, the harmonic wave solution of the jth unit cell can be assumed as

$$U_1^{(j)} = A_1^{(j)} e^{i(jqL - \omega t)}. \tag{4}$$

In equation (4), $U_1^{(j)}$ is the displacement of mass M in the jth unit cell, $A_1^{(j)}$ is the amplitude of displacement $U_1^{(j)}$, q represents the wavenumber, and ω is the angular frequency. By substituting equation (4) into equation (3), the dispersion relation between q and ω reads

$$\omega^2 = \frac{2K(1+\cos(qL)) + 2G(1-\cos qL)\gamma^2}{M + m\left((1+\gamma^2) + (1-\gamma^2)\cos qL\right)}(1-\cos qL). \tag{5}$$

In equation (5), the maximum value of frequency inside the irreducible Brillouin zone ($0 \leqslant qL \leqslant \pi$) is defined as the cut-off frequency, and beyond which no wave could propagate.

The dispersion relation of a standard monoatomic chain [27] composed of masses m^* and springs K^* can be expressed as $\omega^2 = 2K^*(1-\cos qL)/m^*$. The denominator m^* is the inertial part of a general monoatomic chain, which is equal to the actual mass of one unit cell. Similarly, the denominator $M + m((1+\gamma^2) + (1-\gamma^2)\cos qL)$ in equation (5) is defined as the effective inertial part of the 1DOF SMT chain. It could be concluded that the effective inertial part is greater than or equal to the actual mass $M + 2m$ when $\gamma > 1$, i.e. $\alpha < \pi/4$. The inertial amplification factor is defined as

$$I_\mathrm{a} = \frac{M + m\left(\left(1+\gamma^2\right) + \left(1-\gamma^2\right)\cos qL\right)}{M + 2m}. \tag{6}$$

The inertial amplification factor can be made arbitrarily large by increasing the geometrical parameter γ, i.e. decreasing the angle α. However, a small angle does not mean a low cut-off frequency since the numerator in equation (5) also increases with the decrease of angle α if the shear stiffness G is considered. Similarly, the stiffness amplification factor is defined as

$$S_\mathrm{a} = \frac{K(1+\cos(qL)) + G(1-\cos qL)\gamma^2}{K}. \tag{7}$$

The effect of inertial amplification on reducing cut-off frequency is weakened due to the existence of stiffness amplification factor caused by shear stiffness. Broad low bandgaps are harder to obtain due to the existence of transverse shear modes, which is an indispensable material property in solids [31]. Therefore, it is significant to consider the shear stiffness and seek the lowest cut-off frequency under its effect.

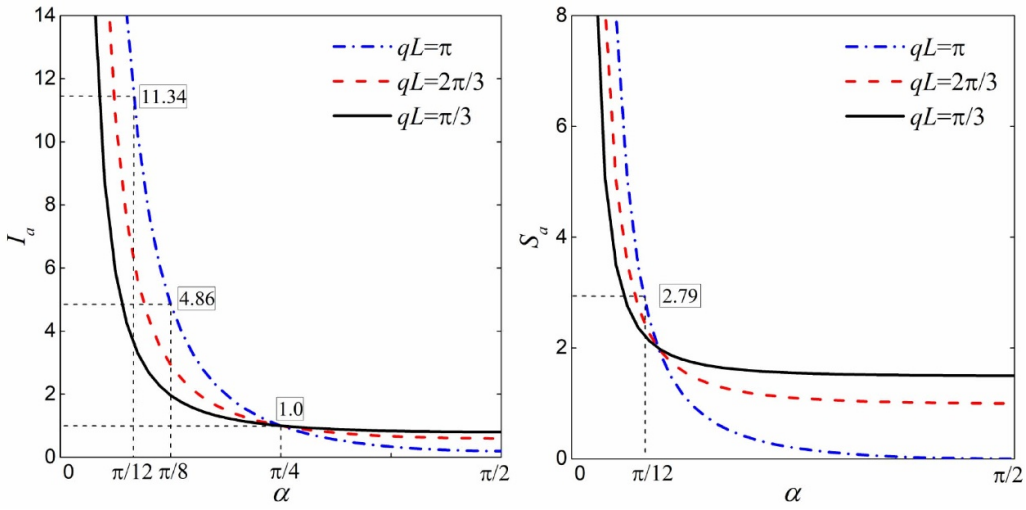

Figure 2. Variation of (a) inertial amplification factor with the angle; (b) stiffness amplification factor with the angle.

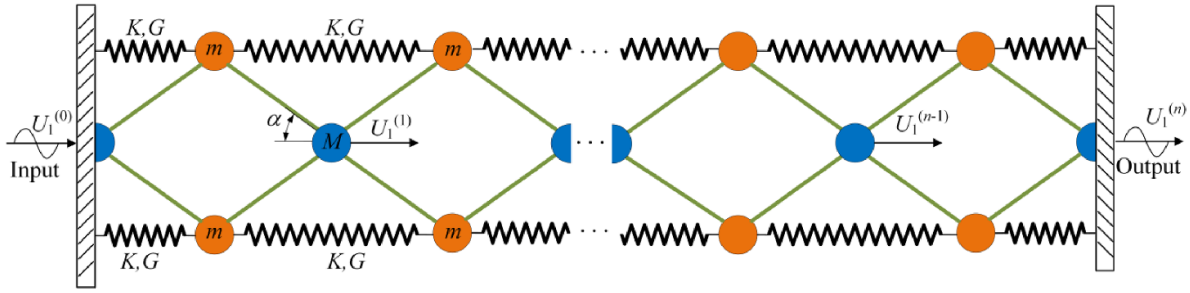

Figure 3. Schematic of n layer finite periodic structure of 1DOF SMT chain. Both ends are fixed on the plate and $U_1^{(0)}$ is a time-harmonic excitation.

The cut-off frequency of the 1DOF SMT chain is strongly associated with the inertial amplification factor in equation (6) and stiffness amplification factor in equation (7). The dependence of two amplification factors on parameters is discussed in figure 2.

Figure 2(a) shows the relations between the inertial amplification factor and angle α with $M = 1$ Kg and $m = 2$ Kg. The inertial amplification factor decreases with the increase of angle α, which is greater than 1 when $\alpha < \pi/4$ for all wavenumbers in figure 2(a). For example, it increases from 4.86 to 11.34 with the angle decreases from $\pi/8$ to $\pi/12$ when $qL = \pi$.

Figure 2(b) shows the variation of stiffness amplification factor with the angle in the case of $K = 1 \times 10^7\ \mathrm{N\,m^{-1}}$ and $G = 1 \times 10^6\ \mathrm{N\,m^{-1}}$. The stiffness amplification factor is only 2.79 with $\alpha = \pi/12$ and $qL = \pi$, which is smaller than the inertial amplification factor 11.34, demonstrating that the 1DOF SMT chain can generate a lower cut-off frequency than the standard monoatomic chain despite the existence of shear stiffness.

To verify the dispersion relation of the above infinite 1DOF SMT chain, response behaviors of the n-period structure subjected to a harmonic excitation are studied. The two ends of the finite period structure are fixed to the plates, as shown in figure 3.

Assume a plane time-harmonic displacement $U_1^{(0)} = A_1^{(0)} e^{-i\omega t}$ is applied to the left base plate as an input excitation. The motion equations of the finite structure can be written as

$$(\mathbf{K} - \omega^2 \mathbf{M})\mathbf{U} = \mathbf{F} \tag{8}$$

where $\mathbf{M} = \mathrm{Diag}[\ M_1 \quad M_2 \quad \ldots \quad M_n\ ]$ is the mass matrix, $\mathbf{K}$ is the generalized stiffness matrix, $\mathbf{U}$ is the displacement vector of middle intersection masses M, $\mathbf{F}$ is the excitation vector as $\mathbf{F} = \mathbf{F}_0 e^{-i\omega t}$.

The vibration transmission is defined as

$$\eta = 20\log_{10}\left|A_1^{(n)} \Big/ A_1^{(0)}\right| \tag{9}$$

where $A_1^{(0)} = 1$ is the displacement amplitude of input excitation at the left end, and $A_1^{(n)}$ is the amplitude of output displacement $U_1^{(n)}$ at the right end.

In the vibration transmission curves, there are some positive peaks and negative peaks, which are rarely explained and computed analytically. In fact, it is the resonance and anti-resonance phenomena of a multi-degree system.

The positive peaks indicate that the output displacement is larger than the input displacement caused by the resonance of the finite structure. Resonance refers to the state that a structure produces the largest possible response to an applied excitation at some specific frequencies, which are the resonance frequencies of the structure. From the perspective of energy conservation, the resonance process is a process of accumulating energy. The accumulated energy comes from the input of external energy before reaching the resonance frequency.

As for the negative peaks in vibration transmission curves, it is caused by the anti-resonance of the finite structure. Anti-resonance refers to the phenomenon that the displacement of a part of the system is significantly small under some specific frequencies excitation, which is an opposite vibration case to the resonance [32].

The resonance and anti-resonance frequencies can be obtained by the motion equations of the finite period structure. For instance, the displacement amplitude of the jth mass M of the n-period structure in figure 3 can be expressed as

$$A_1^{(j)} = \Delta_j(\omega)/\Delta(\omega)\ (j = 1, 2, \cdots, n) \tag{10}$$

where $\Delta(\omega)$ is the determinant of the eigenvalue matrix $\mathbf{D} = \mathbf{K} - \omega^2\mathbf{M}$ in equation (8). Meanwhile, $\Delta_j(\omega)$is the determinant of a matrix obtained by replacing the jth column element of the eigenvalue matrix $\mathbf{D}$ with excitation amplitude vector $\mathbf{F}_0$.

It is obvious that the amplitude $A_1^{(j)}$ tends to be infinite if the denominator $\Delta(\omega) = 0$ in equation (10). Hence, the solution of $\Delta(\omega) = 0$ corresponds to resonance frequencies of the structure. The number of resonance frequencies is equal to the number of DOF of the finite periodic structure.

In contrast, the monitor $\Delta_j(\omega) = 0$ indicates that the jth mass is almost static, the solution of which has $n-1$ positive roots for an n-DOF system and corresponds to the anti-resonance frequencies of the jth mass. However, it is worth noting that only the positive real root is the anti-resonance frequency of the structure.

2.2. Numerical results

In this subsection, the band structure of the 1DOF SMT chain is studied by the dispersion relation in equation (5), and the vibration transmission of finite periodic system in figure 3 with 16 units also is computed by equation (9) to verify the dispersion relation.

Figure 4 shows the dispersion curve and transmission curve of the 1DOF SMT chain with the parameters in table 1. In addition, the cut-off frequency of a standard monoatomic chain is also plotted in figure 4 to evaluate the performance of the SMT chain on low-frequency vibration attenuation. The mass of the monoatomic chain $m^* = M + 2m = 5$ Kg is selected as the total mass of the SMT chain, and the tensile stiffness is assuming as $K^* = 2K = 2 \times 10^7\ \mathrm{N\,m^{-1}}$ since two springs at the bottom and top in figure 1 are connected in parallel.

In figure 4(a), the cut-off frequency of the 1DOF SMT chain (440.8 Hz) is much lower than that of the standard monoatomic chain (636.6 Hz) duo to the inertial amplification. In figure 4(b), the transmission curve of the SMT chain is in black solid curve and it is smaller than zero at frequencies above the cut-off frequency, which agrees well with the dispersion curve predicted by Bloch's theorem. The purple dashed lines in figure 4(b) represent 16 resonance frequencies obtained by the denominator $\Delta(\omega) = 0$ in equation (10), which strictly correspond to the resonance peaks in the transmission curve. Specific values of each order resonance frequency are listed in table 2.

As the transmission curve in figure 4(b) describes the displacement amplitude of the last mass in the right end, only anti-resonance frequencies of $A_1^{(16)}$ should be computed by the numerator $\Delta_{16}(\omega) = 0$ in equation (10). However, the solution of $\Delta_{16}(\omega) = 0$ for anti-resonance only has one positive real root $f = 490.5$Hz (red dash-dot line) in figure 4(b), which falls in the Bragg bandgap, causing the strongest vibration attenuation and reaching -150 dB.

Then, figures 4(c) and (d) demonstrate the effect of shear stiffness on the band structure and transmittance curve with a smaller shear stiffness $G = 1 \times 10^6\ \mathrm{N\,m^{-1}}$ and other material properties keep the same as table 1. As a result, the cut-off frequency of the 1DOF SMT chain in figure 4(c) (234.5 Hz) is much lower than that in figure 4(a) (440.8 Hz), which is only 36.8% of the monoatomic chain (636.6 Hz), illustrating advantages of the SMT chain on the low-frequency vibration attenuation and bandgap regulation. It is noted that the cut-off frequency in figure 4(c) does not appear at $qL = \pi$ and the dispersion curve presents negative group velocity, which will be discussed in the next subsection.

Figure 4(d) presents 15 negative peaks in the transmittance curve, which strictly correspond to the 15 anti-resonance frequencies obtained by the solution of $\Delta_{16}(\omega) = 0$ (red dash-dot lines). The values of 15 anti-resonance frequencies are listed in table 3. The attenuation peak in figure 4(d) reaches -263 dB, which is 75.3% deeper than that in figure 4(b), demonstrating that multiple anti-resonance frequencies in the Bragg bandgap enhance the vibration attenuation of the system.

Different from figure 4, a special case with $G = 0\ \mathrm{N\,m^{-1}}$ and $\alpha = \pi/4$ is concerned, and the dispersion relation and transmission curve are presented in figure 5. Under this specific set of parameters, some interesting phenomena are found in the 1DOF SMT chain.

The dispersion curve in figure 5(a) is symmetric about $qL = \pi/2$ as the dispersion relation in equation (4) can be simplified as $(2m + M)\omega^2 = K(1 - \cos(2qL))$. Therefore, the group velocity is negative when qL is located in $(\pi/2,\ \pi)$, which indicates the energy transmission direction is opposite to the output direction.

In figure 5(b), it is interesting to note that there are only eight resonance peaks in the transmission curve of a 16 DOF finite periodic chain, which is half of the resonance peaks in figures 4(b) and (d). This difference can be explained by the

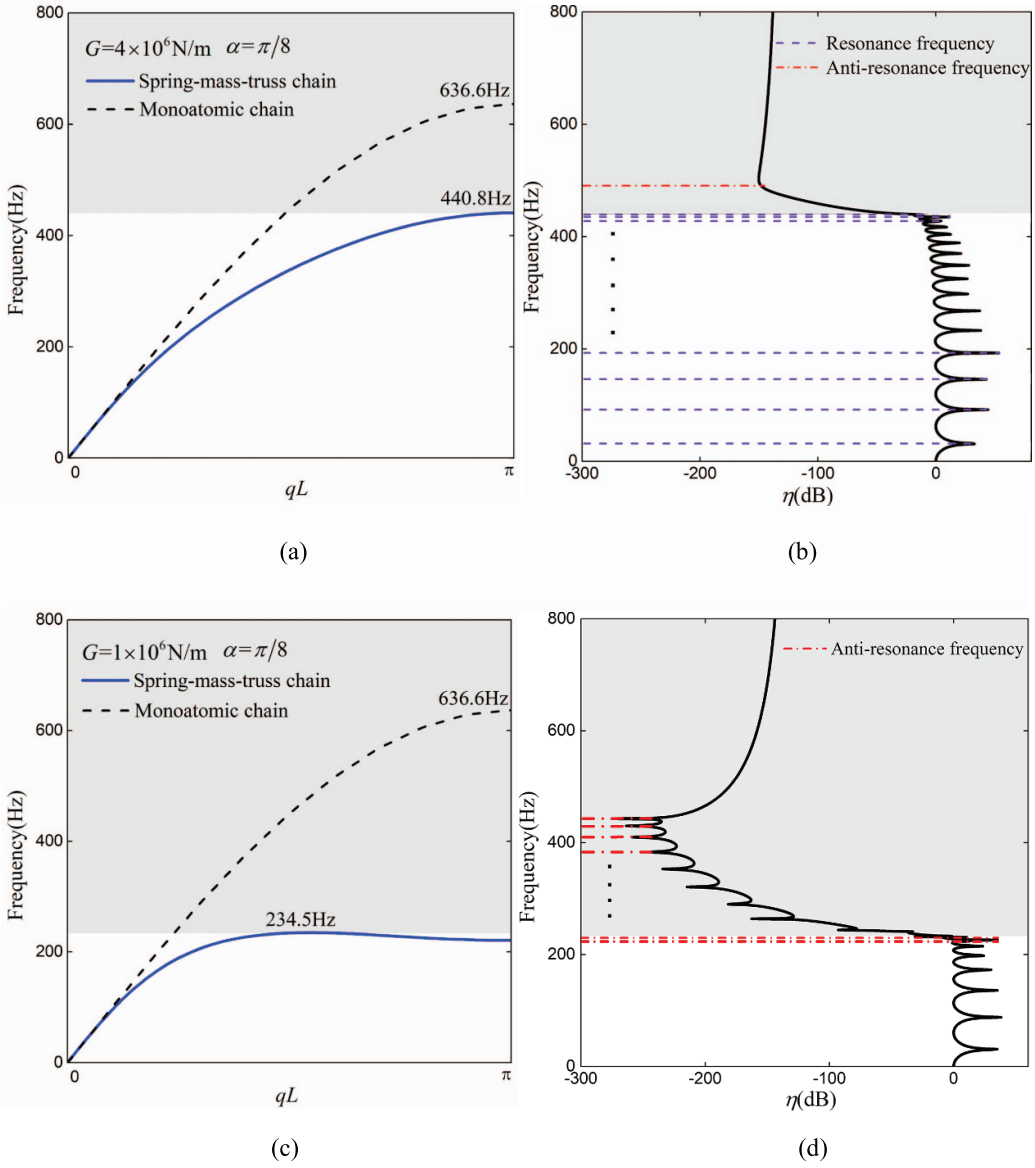

Figure 4. Dispersion relation curves of the 1DOF SMT chain with: (a) the parameters in table 1; (c) the same parameters to (a) except smaller shear stiffness $G = 1 \times 10^6$ N m^{-1}; right-hand panels (b) and (d) are the transmission curves corresponding to (a) and (c). The dispersion curves for the monatomic chain are in black dashed curves.

Table 1. The parameters used in 1DOF SMT chain.

Mass value (Kg)		Stiffness value (N m^{-1})		Angle (rad)
$M = 1$	$m = 2$	$K = 1 \times 10^7$	$G = 4 \times 10^6$	$\alpha = \pi/8$

Table 2. Resonance frequency in figure 4(b).

Item	Resonance frequency (Hz)							
Order	f_1	f_2	f_3	f_4	f_5	f_6	f_7	f_8
Value	32.5	91.9	146.1	193.0	233.1	267.9	298.3	325.3
Order	f_9	f_{10}	f_{11}	f_{12}	f_{13}	f_{14}	f_{15}	f_{16}
Value	349.2	370.3	388.7	404.5	417.4	427.6	434.9	439.3

Table 3. Anti-resonance frequency in figure 4(d).

Item	Anti-resonance frequency (Hz)							
Order	f_1	f_2	f_3	f_4	f_5	f_6	f_7	f_8
Value	222.3	222.3	224.2	224.2	230.1	230.1	233.7	264.0
Order	f_9	f_{10}	f_{11}	f_{12}	f_{13}	f_{14}	f_{15}	/
Value	290.3	320.8	352.8	383.3	409.8	430.2	443.0	/

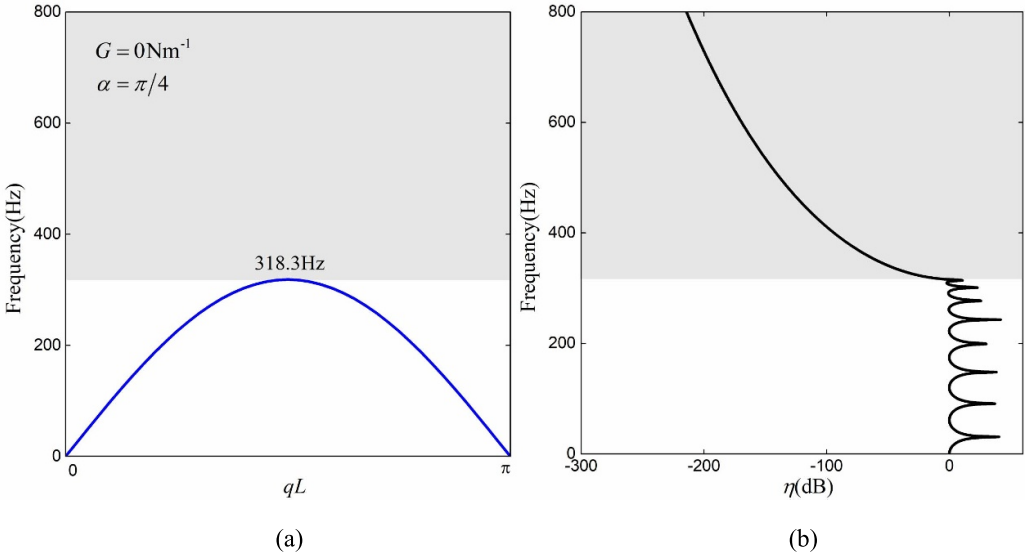

Figure 5. (a) Dispersion relation and (b) transmission curve with $G = 0$ N m^{-1} and $\alpha = \pi/4$.

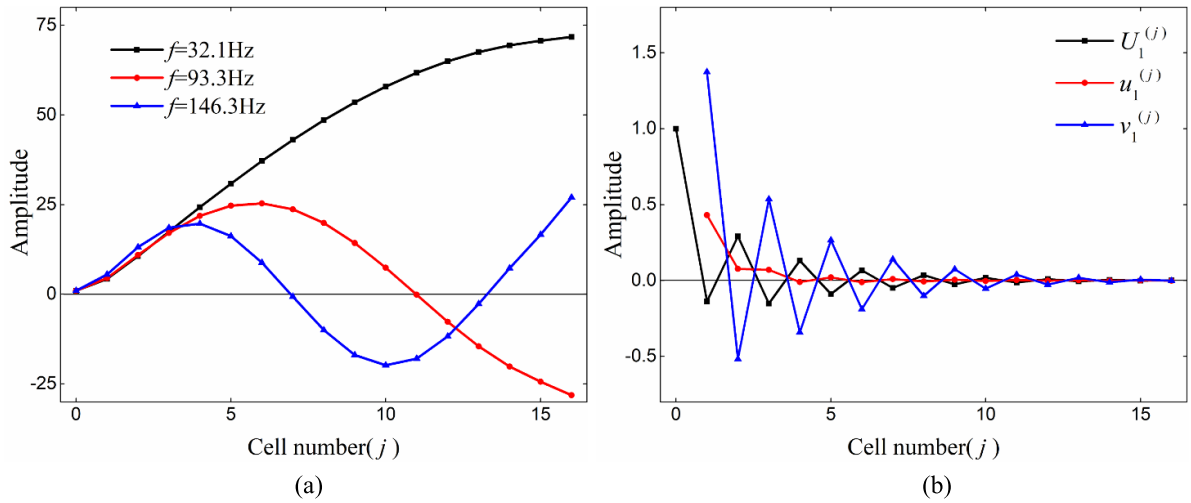

Figure 6. Displacement amplitude field in space of: (a) intersection masses M under the first three order resonance frequencies $f = 32.1$ Hz (black curve), $f = 93.3$ Hz (red curve) and $f = 146.3$ Hz (blue curve); (b) masses M (black curve) and m (red and blue curves represent the amplitude of horizontal and vertical displacement) with $f = 445$Hz above the cut-off frequency.

degeneration of equation (3) with $G = 0$ N m^{-1} and $\alpha = \pi/4$, which can be rewritten as

$$M\frac{\mathrm{d}^2 {U_1}^{(j)}}{\mathrm{d}t^2} + 2m\frac{\mathrm{d}^2 {U_1}^{(j)}}{\mathrm{d}t^2} + \frac{1}{2}K(2{u_1}^{(j)} - {u_1}^{(j+2)} - {u_1}^{(j-2)}) = 0. \tag{11}$$

It can be observed from equation (11) that the motion equation of the jth mass only contains ${U_1}^{(j-2)}$, ${U_1}^{(j)}$ and ${U_1}^{(j+2)}$. As a consequence, the movements of odd masses and even masses are independent with $G = 0$ N m^{-1} and $\alpha = \pi/4$. Hence, there are only eight resonance peaks in the transmission curve and the even masses keep static if only the first mass is excited.

Figure 6 shows the displacement amplitudes of masses to discuss the resonance phenomenon detailly and understand the inertial amplification mechanism clearly with the same parameters as figure 4(b). In figure 6(a), the displacement

amplitudes of all intersection masses M under the first three resonance frequencies are plotted. The vibration of the structure is extremely violent under the resonance frequencies, and the amplitude variation along the cell number is similar to the mode shape of a cantilever beam. Since the right end of the finite periodic system is free, all of the maximum displacement amplitudes appear at the last intersection mass in the right end, which are more than 25 times the input excitation.

Figure 6(b) depicts the displacement amplitudes of masses M and m with $f = 445$ Hz, which is above the cut-off frequency in figure 4(a). $U_1^{(j)}$ denotes the displacement amplitude of jth mass M of the finite periodic structure in figure 3, $u_1^{(j)}$ and $v_1^{(j)}$ represent the horizontal and vertical displacement amplitudes for m in the jth unit respectively. All displacements decay to zero as the number of unit cells increases, which indicates the vibration attenuation along the chain. The vertical vibration of m has the largest amplitude, illustrating that the horizontal displacement of intersection mass M is mainly converted into the vertical motion of m by scissors-like trusses. It can be found from equation (2) that the smaller the angle, the larger the vertical displacement of m, which has the same trend as the amplification effect of inertia in equation (5). Therefore, the inertial amplification mechanism can be understood as the amplification of displacement, i.e. the movement of intersection masses M is converted into amplified vertical movement of vertex masses m by a scissor-like structure.

2.3. Effect of parameters on bandgap

To seek a lower frequency attenuation range by optimizing the structure parameters, the effect of parameters on the cut-off frequency is investigated in detail in this subsection. Basic parameters are selected as $M = 1$ Kg, $K = 1 \times 10^7$ N m^{-1} and dimensionless parameters are defined as $\lambda = G/K$, $\mu = m/M$.

It has been found in figure 4(c) that the cut-off frequency f_{cut} of the 1DOF SMT chain does not always appear at $qL = \pi$. The concept of group velocity is introduced here to get the analytical expression of f_{cut}. In the dispersion $\omega - q$ diagram, the group velocity of a wave group or packet is given by the slope of dispersion curves, i.e. $v_g = \mathrm{d}\omega/\mathrm{d}(qL)$.

The solution of group velocity $v_g = 0$ with respect to wavenumber q can be obtained by the implicit differentiation of equation (5). One of the roots is a constant $qL = \pi$, and the other variable root is defined as q^*, which can be expressed as equation (13). If the variable root q^*in equation (13) satisfies $0 < q^*L < \pi$, the obtained wave number q^* corresponds to the cut-off frequency. Otherwise, the cut-off frequency appears at $qL = \pi$ (including $\lambda = 1/\gamma^2$ in equation (13))

$$\cos(q^*L) = \begin{cases} \dfrac{\left(\lambda\gamma^2 - 1\right)\left(1 + \mu + \mu\gamma^2\right) + \sqrt{\psi}}{\mu\left(\gamma^2 - 1\right)\left(\lambda\gamma^2 - 1\right)} & \gamma^2 \neq 1 \;\&\&\; \dfrac{1}{\lambda} \\ \dfrac{\lambda}{\lambda - 1} & \gamma^2 = 1 \end{cases} \tag{12}$$

where $\psi = (1 + 2\mu)\left(\lambda\gamma^2 - 1\right)\left(\left(\lambda + 2(\lambda - 1)\mu\right)\gamma^2 - 1\right)$.

The critical stiffness ratio λ_{cr} making $0 < q^*L < \pi$ can be solved by the expression in equation (12). By substituting $qL = q^*L$ $(\lambda < \lambda_{\text{cr}})$ and $qL = \pi$ $(\lambda \geqslant \lambda_{\text{cr}})$ into equation (5), the piecewise function f_{cut} can be determined as

$$f_{\text{cut}} = \begin{cases} \dfrac{2\sqrt{2\lambda\gamma^2}}{\sqrt{1 + 2\mu\gamma^2}} f_0 & \lambda \geqslant \lambda_{\text{cr}} \\ 2\sqrt{\dfrac{\left(1 + \mu + (\mu - \lambda(1 + 2\kappa))\gamma^2 - \sqrt{\psi}\right)}{\mu^2\left(\gamma^2 - 1\right)^2}} f_0 & \lambda < \lambda_{\text{cr}} \\ \sqrt{\dfrac{2}{(1 - \lambda)(1 + 2\mu)}} f_0 & \lambda < \lambda_{\text{cr}} \;\&\&\; \gamma = 1 \end{cases} \tag{13}$$

where $f_0 = \frac{\sqrt{K/M}}{2\pi}$ and $\lambda_{\text{cr}} = \frac{1 + 2\mu\gamma^2}{2\gamma^2(1 + \mu + \mu\gamma^2)}$.

Each curve in figure 7 depicts the variation of cut-off frequency f_{cut} with assembly angle α under different stiffness ratios λ and mass ratios μ. Firstly, the cut-off frequency shifts to lower frequency with the increase of mass ratio from $\mu = 0.5$ (in blue dash-dotted curves) to $\mu = 2$ (in red dashed curves) and then to $\mu = 4$ (in black solid curves) in each subfigure of figure 7.

Then, the effect of shear stiffness is investigated by assuming $\lambda = 0.05$, 0.2 and 0.4 from figures 7(a)–(c) as the maximum of shear stiffness is constrained by the relation between three elastic constants of isotropic material. Intuitively, the cut-off frequency f_{cut} increases with the stiffness ratio λ.

Figure 7 shows the cut-off frequency f_{cut} is sensitive to angle, indicating that the angle α is a crucial design parameter. In general, f_{cut} first decreases before inflection points (in red triangle markers) and then increases with angle α. The inflection points in figure 7 represent the minimum value of f_{cut}, which means the lowest vibration attenuation frequency range. It is interesting to notice that the lowest cut-off frequency is near to the black circle marker in figure 7, which is the piecewise point of the piecewise function f_{cut} at $\lambda = \lambda_{\text{cr}}$. Therefore, the piecewise point can be obtained by the expression of λ_{cr} to predict the value and location of the lowest cut-off frequency.

3. 2DOF spring–mass–truss (SMT) chain

In the previous section, there is only one dispersion curve in the 1DOF SMT chain and the low cut-off frequency is desired for low-frequency vibration attenuation. Other than decreasing the cut-off frequency, increasing the number of bandgaps is another effective method to lower and widen the vibration attenuation range. One method of increasing bandgap is to attach some resonators according to the Locally Resonant mechanism. The other is based on the Bragg Scattering mechanism, i.e. a bandgap can be generated by using different materials to adjust elastic waves. For the discrete mass models, a heterogeneous medium for generating Bragg bandgap can be achieved by changing adjacent mass, connection stiffness, or geometric parameters.

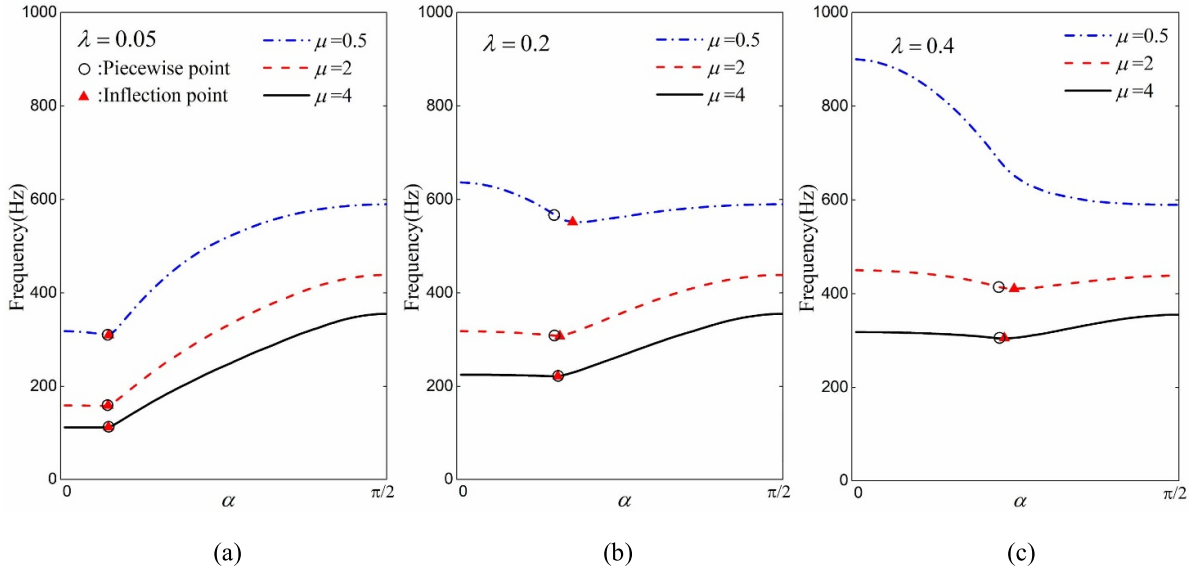

Figure 7. Variation of the cut-off frequency with angle α under different mass ratios μ when: (a) stiffness ratios $\lambda = 0.05$; (b) $\lambda = 0.2$; (c) $\lambda = 0.4$. The red triangle marker is the inflection point of cut-off frequency and the black circle marker is the piecewise point of piecewise function f_{cut}.

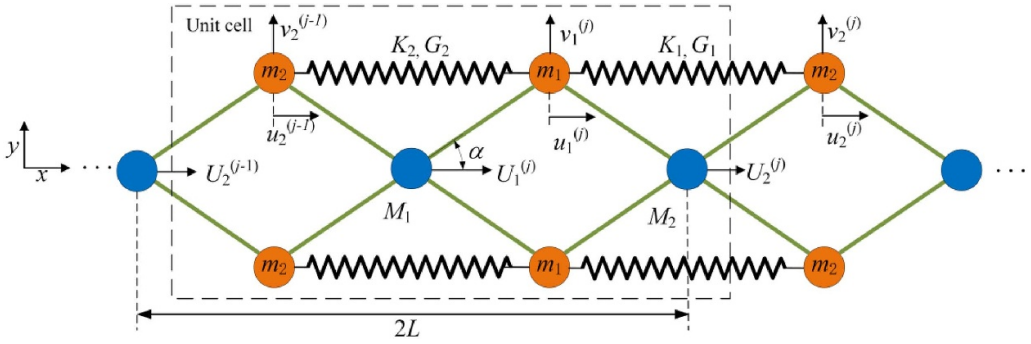

Figure 8. Infinite periodic 2DOF SMT chain.

3.1. Dispersion relation analysis

In this section, the 2DOF SMT chain is proposed in figure 8 to generate a lower bandgap. It is modified from the 1DOF SMT chain by varying the masses and springs of two adjacent basic units alternatively, resulting in the lattice constant becoming $2L$. One unit cell in figure 8 consists of two main masses M_1 and M_2in the middle intersection, two diatomic chains in the upper and lower chain separately, as shown in the dashed box. Each diatomic chain is composed of masses m_1 and m_2, springs K_1 (with shear stiffness G_1) and K_2 (with shear stiffness G_2).

The equations of motion can be given by

$$
\begin{aligned}
&M_1\frac{\mathrm{d}^2U_1^{(j)}}{\mathrm{d}t^2}+m_1\frac{\mathrm{d}^2u_1^{(j)}}{\mathrm{d}t^2}+m_1\frac{\mathrm{d}^2v_1^{(j)}}{\mathrm{d}t^2}\gamma+m_2\frac{\mathrm{d}^2u_2^{(j-1)}}{\mathrm{d}t^2}\\
&-m_2\frac{\mathrm{d}^2v_2^{(j-1)}}{\mathrm{d}t^2}\gamma+K_1\left(u_1^{(j)}-u_2^{(j)}\right)+K_1\left(u_2^{(j-1)}-u_1^{(j-1)}\right)\\
&+G_1(v_1^{(j)}-v_2^{(j)})\gamma+2G_2\left(v_1^{(j)}-v_2^{(j-1)}\right)\gamma\\
&-G_1\left(v_2^{(j-1)}-v_1^{(j-1)}\right)\gamma=0
\end{aligned}
$$

$$
\begin{aligned}
&M_2\frac{\mathrm{d}^2U_2{}^{(j)}}{\mathrm{d}t^2}+m_2\frac{\mathrm{d}^2u_2^{(j)}}{\mathrm{d}t^2}+m_2\frac{\mathrm{d}^2v_2^{(j)}}{\mathrm{d}t^2}\gamma+m_1\frac{\mathrm{d}^2u_1^{(j)}}{\mathrm{d}t^2}\\
&-m_1\frac{\mathrm{d}^2v_1^{(j)}}{\mathrm{d}t^2}\gamma+K_2\left(u_2^{(j)}-u_1^{(j+1)}\right)+K_2\left(u_1^{(j)}-u_2^{(j-1)}\right)\\
&+G_2\left(v_2^{(j)}-v_1^{(j+1)}\right)\gamma+2G_1\left(v_2^{(j)}-v_1^{(j)}\right)\gamma\\
&-G_2\left(v_1^{(j)}-v_2^{(j-1)}\right)\gamma=0.
\end{aligned}
\tag{14}
$$

By using ansatz $U_{1,2}^{(j)}=A_{1,2}e^{i(2jqL-\omega t)}$ and small displacements assumption, the equations of motion can be written in the following matrix form

$$
\begin{pmatrix} B_{11} & B_{12} \\ B_{21} & B_{22} \end{pmatrix}\begin{pmatrix} A_1 \\ A_2 \end{pmatrix}=\begin{pmatrix} 0 \\ 0 \end{pmatrix} \tag{15}
$$

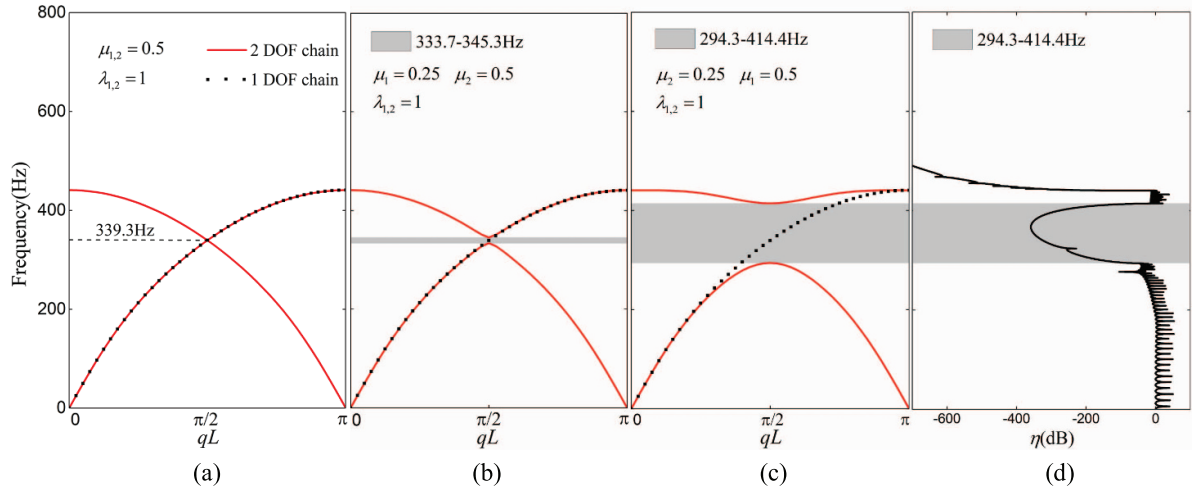

Figure 9. Dispersion relation of 2DOF SMT chain with: (a) $\mu_{1,2}=0.5$, $\lambda_{1,2}=1$; (b) $\mu_1=0.25$; (c) $\mu_2=0.25$; (d) is the transmission curve corresponding to (c). The black dot curves are the dispersion relation of the 1DOF SMT chain.

where

$$\begin{cases} B_{11}=2K_1+2\left(2G_2+G_1\right)\gamma^2-\left(2M_1+\left(m_1+m_2\right)\left(1+\gamma^2\right)\right)\omega^2 \\ \qquad -2\left(K_1-G_1\gamma^2\right)\cos(2qL) \\ B_{21}=-m_1\omega^2-\left(2\left(G_1+G_2\right)-m_1\omega^2\right)\gamma^2 \\ \qquad -\mathrm{e}^{-2\mathrm{i}qL}\left(2\left(G_1+G_2\right)\gamma^2-m_2\left(\gamma^2-1\right)\omega^2\right) \\ B_{21}=-m_1\omega^2-\left(2\left(G_1+G_2\right)-m_1\omega^2\right)\gamma^2 \\ \qquad -\mathrm{e}^{2\mathrm{i}qL}\left(2\left(G_1+G_2\right)\gamma^2-m_2\left(\gamma^2-1\right)\omega^2\right) \\ B_{22}=2K_2+2\left(2G_1+G_2\right)\gamma^2-\left(2M_2+\left(m_1+m_2\right)\left(1+\gamma^2\right)\right)\omega^2 \\ \qquad -2\left(K_2-G_2\gamma^2\right)\cos(2qL) \end{cases} \tag{16}$$

The dispersion relation can be obtained by setting the determinant of the coefficient matrix to zero.

The dimensionless parameters are defined as $\mu_1=M_2/\left(M_1+M_2\right)$, $\mu_2=m_2/\left(m_1+m_2\right)$ and $\lambda_1=K_2/K_1$, $\lambda_2=G_2/G_1$. In the numerical analysis, the total mass is fixed as $M_1+M_2=2$ Kg and $m_1+m_2=4$ Kg to seek the better mass configuration without an additional increase of the system mass. Basic parameters are selected as: $K_1=1\times10^7$ N m^{-1}, $G_1=4\times10^6$ N m^{-1} and $\alpha=\pi/8$.

Figure 9 shows the dispersion curves of the 2DOF SMT chain with different mass ratios μ_1 and μ_2. Meanwhile, the black dotted curves are the dispersion curves of the 1DOF SMT chain. In figure 9(a), adjacent parameters of the 2DOF SMT chain are the same as table 1 ($\mu_{1,2}=0.5$, $\lambda_{1,2}=1$), resulting in the structure in figure 8 being reduced to the 1DOF SMT chain. However, a supercell is formed due to the lattice constant shifts from L to $2L$, and the Irreducible Brillouin zone becomes $(0,\pi/2L)$. Therefore, the dispersion curves of the 2DOF SMT chain have two branches, which can be obtained by folding the dispersion curve of the 1DOF chain about $\pi/2$ at 339.3 Hz.

In figure 9(b), only two adjacent intersection masses $M_{1,2}$ are changed as $\mu_1=0.25$, i.e. $M_1=1$ Kg and $M_2=3$ Kg. The wave propagation speed is low in heavy or soft mediums but high in light or hard mediums, resulting in the separation of two branches and the generation of a bandgap at 333.7 Hz–345.3 Hz. The mass distribution of m_1 and m_2 has less effect on opening the bandgap. In the following analysis, keep $M_1=M_2=1$ Kg unless otherwise stated.

Similar to figure 9(b), we solely change adjacent vertex masses $m_{1,2}$ as $\mu_2=0.25$ in figure 9(c). It is shown that changing different adjacent parameters has different performance on opening bandgap. The bandgap width with the same parameter ratio in figure 9(c) ($\mu_2=0.25$) is 120.1 Hz, while the width of the bandgap in figure 9(b) ($\mu_1=0.25$) is 11.6 Hz. Moreover, both bandgaps in figures 9(b) and (c) are below the cut-off frequency of the 1DOF chain, illustrating that it is a practical method to generate an aimed bandgap.

The corresponding transmission curve to figure 9(c) is plotted in figure 9(d). In the simulations, the finite periodic system is composed of 40 unit cells and the vibration attenuation range is in great agreement with the bandgap in figure 9(c).

In figure 9, there is a bandgap between the lower and upper branches, which does not exist in the 1DOF SMT chain. Figure 1 illustrates the displacement amplitude in spacial fields of intersection masses M with the excitation frequencies $f=100$Hz and $f=440.7$Hz, which are at the first and second branches in figure 9(c) respectively. The red and blue markers represent the odd and even number intersection masses M. It is evident that two neighboring intersection masses move in phase at the lower dispersion curve (acoustic branch) in figure 10(a) and out of phase at the upper curve (optical branch) in figure 10(b), respectively.

The generation of bandgap in figure 9 is mainly benefited from the separation of acoustic and optical branches at $qL=\pi/2$, in which the values are defined as f_{bou1} and f_{bou2}. Nevertheless, the width of the bandgap also depends on the starting value of the optical branch at $qL=0$, which is defined as f_{bou3}.

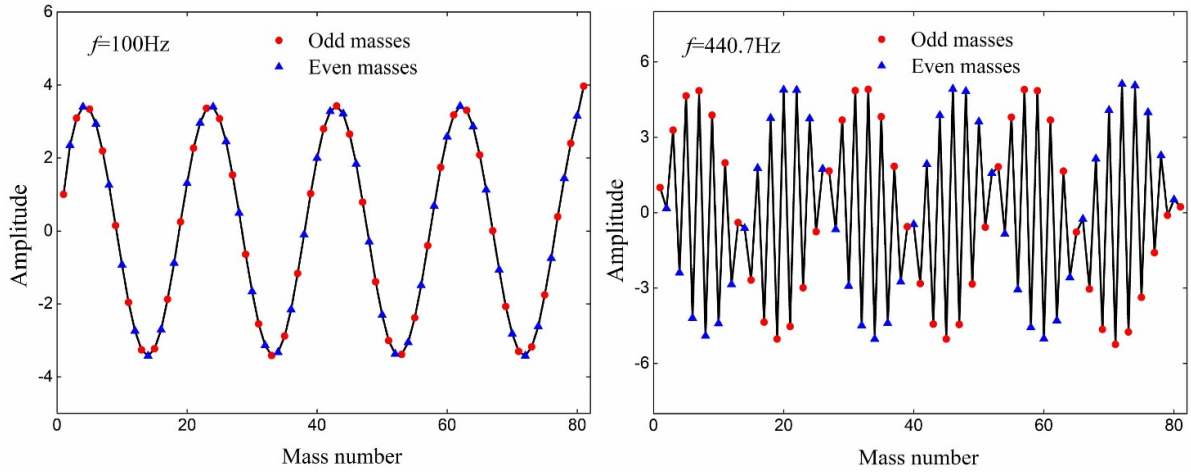

(a) (b)

Figure 10. Displacement amplitude of intersection masses M in space with 40 unit cells at: (a) the acoustic branch $f = 100$Hz; (b) the optical branch $f = 440.7$Hz in figure 9(c).

Three decisive values for the existence and width of bandgap can be expressed as

$$\begin{aligned} f_{\text{bou1}} &= f_{\text{acoustic}}\big|_{qL=\pi/2} = \frac{1}{2\pi}\sqrt{\frac{\varphi_1 - \sqrt{{\varphi_1}^2 - 4\varphi_2\varphi_3}}{2\varphi_2}} \\ f_{\text{bou2}} &= f_{\text{optical}}\big|_{qL=\pi/2} = \frac{1}{2\pi}\sqrt{\frac{\varphi_1 + \sqrt{{\varphi_1}^2 - 4\varphi_2\varphi_3}}{2\varphi_2}} \\ f_{\text{bou3}} &= f_{\text{optical}}\big|_{qL=0} = \frac{\gamma}{2\pi}\sqrt{\frac{5G_1(1+\lambda_2)}{(1+\mu_1-\mu_1^2)+\gamma^2}} \end{aligned} \tag{17}$$

where

$$\begin{aligned} \varphi_1 &= K_1\left(1+\mu_1+\gamma^2\right) + K_1\left(2-\mu_1+\gamma^2\right)\lambda_1 \\ &\quad + G_1\gamma^2\left(2+\mu_1(\lambda_2-1)+\lambda_2+\gamma^2(1+\lambda_2)\right) \\ \varphi_2 &= 1-(\mu_1-1)\mu_1+5\gamma^2-4(\mu_2-1)\mu_2\left(\gamma^2-1\right)^2 \\ \varphi_3 &= \left(K_1\lambda_1+G_1\gamma^2\right)\left(K_1+G_1\gamma^2\lambda_2\right). \end{aligned} \tag{18}$$

According to equation (17), it turns out that the starting value of the optical branch f_{bou3} is closely related to the shear stiffness $G_1(1+\lambda_2)$. The width of the 2DOF SMT chain bandgap will be severely affected if f_{bou3} in figure 9(a) is too small or even lower than f_{bou1}. Specifically, $f_{\text{bou3}} = 0$ when $G_1 = G_2 = 0$, and there is no bandgap no matter what other parameters are selected. It is suggested to generate a bandgap by changing adjacent parameters when $f_{\text{bou3}} > f_{\text{bou1}}$. The critical shear stiffness G_{cr} for the condition of bandgap existence $f_{\text{bou3}} = f_{\text{bou1}}$ can be obtained from equation (17), as shown in equation (20)

$$G_{\text{cr}} = \frac{\left(M+2m\gamma^2\right)K}{\gamma^2\left(3M+4m+2m\gamma^2\right)}. \tag{19}$$

3.2. Effect of parameters on bandgap

To optimize the structure parameters for better performance on low-frequency vibration attenuation, the influence of parameters including the mass ratio, tensile stiffness ratio, shear stiffness ratio, and angle is analyzed in this subsection.

As shown in figure 11, the blue dashed, black dash-dot and red solid lines represent three decisive values f_{bou1}, f_{bou2} and f_{bou3} in equation (17), respectively. Meanwhile, the shaded area is the actual bandgap range.

Figure 11(a) demonstrates the dependence of bandgap boundary frequencies on the mass ratio μ_2, and other adjacent parameters are the same as table 1. Furthermore, the case of $M_{1,2} = 0$ is also considered to discuss the effect of intersection masses M, which is presented by the curves with circle markers. The difference of bandgap boundary is very small between $M_{1,2} = 0$ and $M_{1,2} = 1$ Kg (in curves without circle markers), thus the presence of intersection masses M is meaningless for the bandgap generation.

In figure 11(a), there is no bandgap with $\mu_2 = 0.5$ because the acoustic and optical branches intersect at 339.3 Hz, as shown in the dispersion curves in figure 9(a). With the mass ratio μ_2 away from $\mu_2 = 0.5$, the acoustic branch goes down from 339.3 Hz at $qL = \pi/2$ as one of m_1 and m_2 becomes heavier, which is reflected in the decrease of f_{bou1}. Meanwhile, the optical branch goes up from 339.3 Hz as the other of m_1 and m_2 becomes lighter, which is reflected in the increase of f_{bou2}. The variation trend of the bandgap is that the greater the difference between m_1 and m_2, the lower and wider the bandgap, until f_{bou2} reaches f_{bou3}.

The variation of bandgap boundary frequencies with different tensile stiffness ratios λ_1 and shear stiffness ratios λ_2

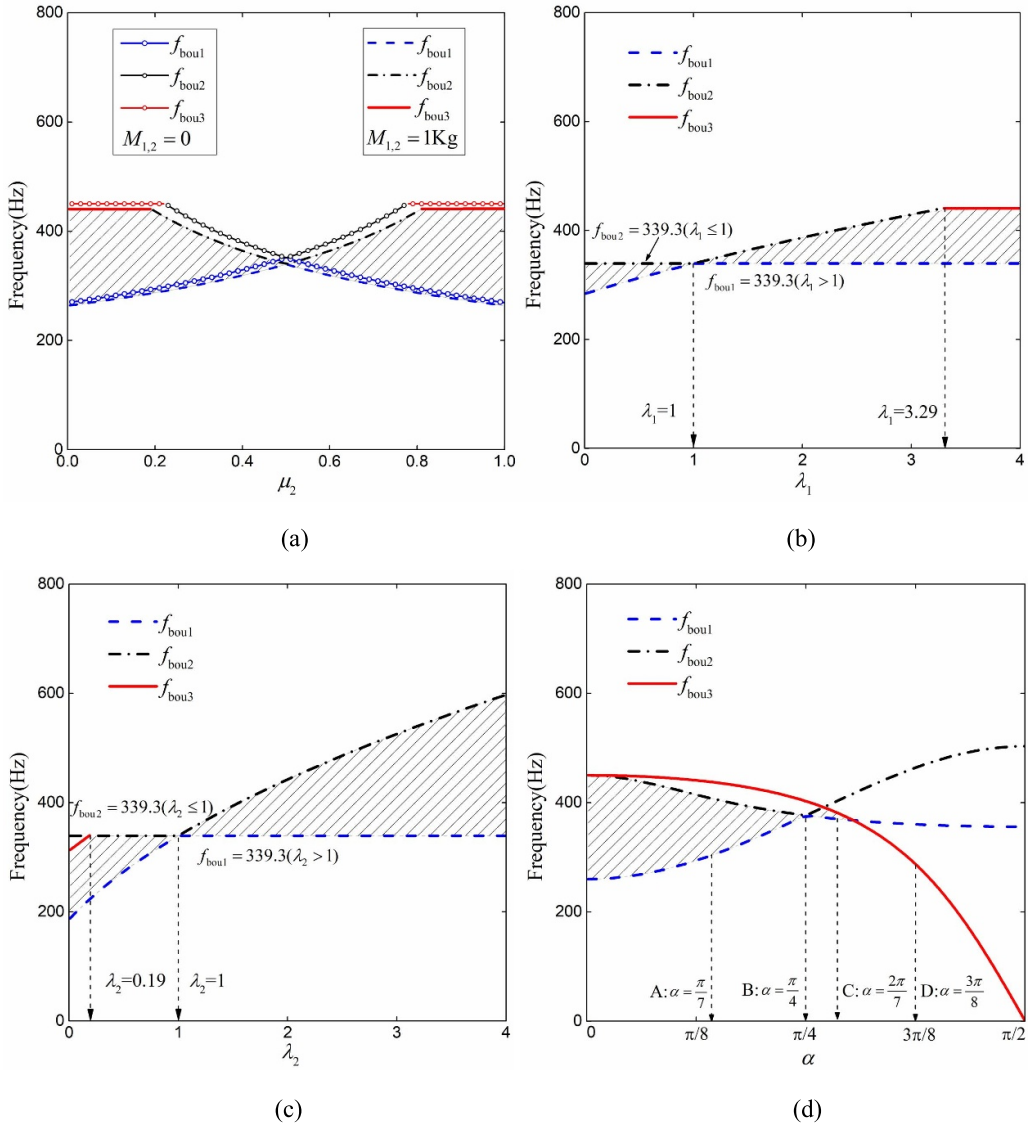

Figure 11. Variation of bandgap boundary frequencies with different: (a) mass ratios μ_2; (b) tensile stiffness ratios λ_1; (c) shear stiffness ratios λ_2; (d) angle α when $\mu_2 = 0.25$.

are then characterized in figures 11(b) and (c). Similar to figure 11(a), there is no bandgap with $\lambda_1 = 1$ or $\lambda_2 = 1$, as the acoustic and optical branches intersect at 339.3 Hz, i.e. $f_{\text{bou1,2}} = 339.3$Hz. However, this intersection frequency $f =$ 339.3Hz is unchanged with λ_1 and λ_2 in figures 11(b) and (c), illustrating that one of the acoustic and optical branches remains constant at $qL = \pi/2$.

In figures 11(b) and (c), the expressions of f_{bou1} and f_{bou2} can be rewritten as equation (21)

$$f_{\text{bou1}} = \begin{cases} \dfrac{1}{2\pi}\sqrt{\dfrac{(1.5+\gamma^2)\,2\,(G_1\gamma^2+K_1\lambda_i)}{1.25+5\gamma^2+(\gamma^2-1)^2}}, & \lambda_i \leqslant 1 \\ 339.3\text{Hz}\,, & \lambda_i > 1 \end{cases}$$

$$f_{\text{bou2}} = \begin{cases} 339.3\text{Hz}\,, & \lambda_i \leqslant 1 \\ \dfrac{1}{2\pi}\sqrt{\dfrac{(1.5+\gamma^2)\,2\,(G_1\gamma^2+K_1\lambda_i)}{1.25+5\gamma^2+(\gamma^2-1)^2}}, & \lambda_i > 1 \end{cases} \tag{20}$$

where $i = 1$ in figure 11(b) and $i = 2$ in figure 11(c).

It can be found $f_{\text{bou1}} = 339.3$Hz with $\lambda_1 > 1$ or $\lambda_2 > 1$ and $f_{\text{bou2}} = 339.3$Hz with $\lambda_1 \leqslant 1$ or $\lambda_2 \leqslant 1$ in equation (20). Compared with the parameters in table 1, spring K_2 is softer when $\lambda_1 \leqslant 1$ or $\lambda_2 \leqslant 1$. Therefore, the acoustic branch goes down with a softer medium and the optical branch remains constant as the coefficient of spring K_1 is fixed. Conversely, the optical branch goes up and the acoustic branch remains constant with a harder medium when $\lambda_1 > 1$ or $\lambda_2 > 1$. The width of the bandgap increases with shear stiffness ratios $\lambda_{1,2}$ away from $\lambda_{1,2} = 1$ until $\lambda_1 > 3.29$ in figure 11(b) and $\lambda_2 < 0.19$ in figure 11(c).

Figure 11(d) discusses the effect of assembly angle α on the bandgap with $\mu_2 = 0.25$, $\mu_1 = 0.5$ and $\lambda_{1,2} = 1$. The smaller the angle α, the lower and wider the bandgap when $\alpha < \pi/4$. Therefore, it is easier to generate a bandgap when the SMT chain has inertial amplification, as the inertial amplification factor in figure 2(a) is greater than 1 only when $\alpha < \pi/4$.

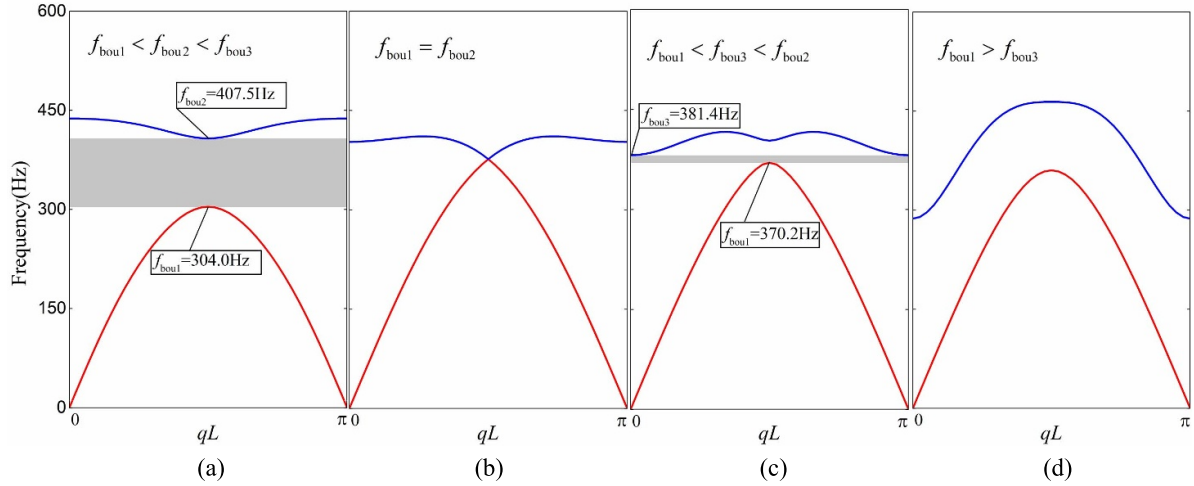

Figure 12. Dispersion relation curves at points A, B, C, and D in figure 11(d) with: (a) $\alpha = \pi/7$; (b) $\alpha = \pi/4$; (c) $\alpha = 2\pi/7$; (d) $\alpha = 3\pi/8$.

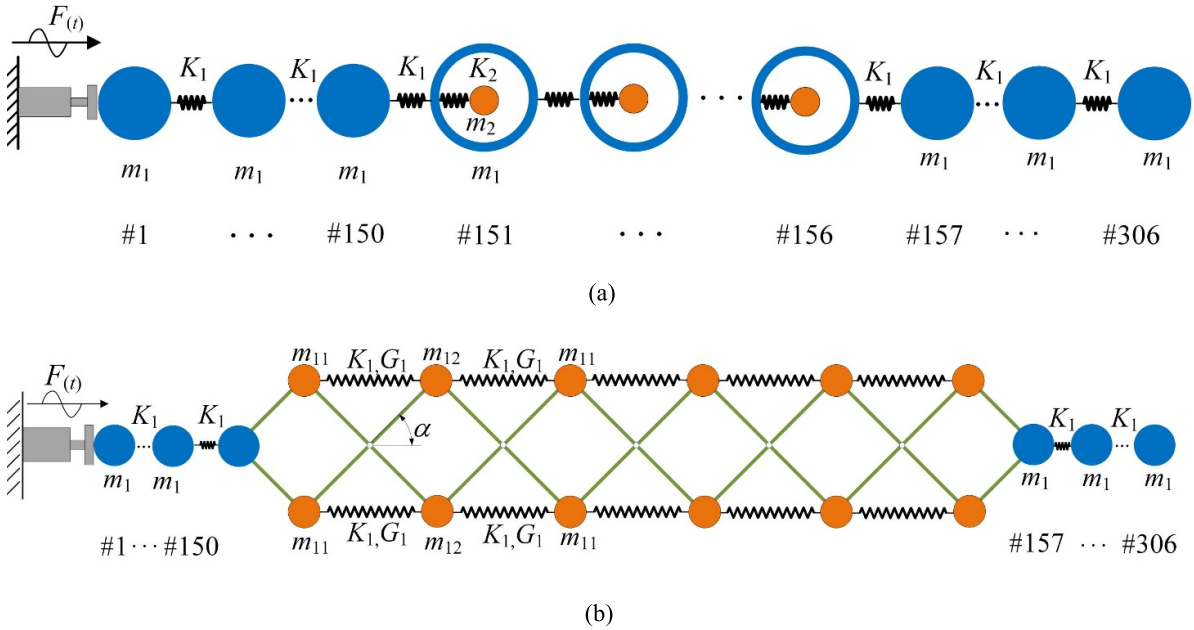

Figure 13. Finite chain structure containing: (a) six unit cells of classic local resonance system; (b) three unit cells of the 2DOF SMT chain. Both ends are finite monatomic chains of length 150.

In figure 11, the upper boundary of the bandgap is lower than the cut-off frequency of the 1DOF chain $f_{cut} = 440.8$Hz except for the right part of figure 11(c) with large shear stiffness ratios λ_2. The desired broad low bandgap can indeed be obtained by tuning the structure parameters.

The shape of the dispersion curves varies with the structure parameters, which are mainly reflected in the order of three frequencies f_{bou1}, f_{bou2} and f_{bou3}. Figure 12 shows the wave dispersion curves of the 2DOF SMT chain with different angles at points A, B, C, and D in figure 11(d). In figure 12(a), f_{bou2} determines the upper boundary of the bandgap, and the optical branch is concave. Particularly, no bandgap in figure 12(b) due to $f_{bou1} = f_{bou2}$ with $\alpha = \pi/4$. As f_{bou3} drops with the increase of angle, the widths of bandgaps in figures 12(c) and (d) are severely affected despite the separation of the acoustic and optical branches.

3.3. *Transient analysis under the action of wavelet packet*

Based on the parameter analysis in section 3.2, the wide bandgap below the cut-off frequency can be obtained by the 2DOF SMT chain. The vibration in engineering is mostly caused by broadband excitation, and the wave packet is often used to verify the attenuation of structures to broadband waves [24, 33, 34].

In the next, the effectiveness of the proposed structure on broadband wave attenuation is investigated. As shown in

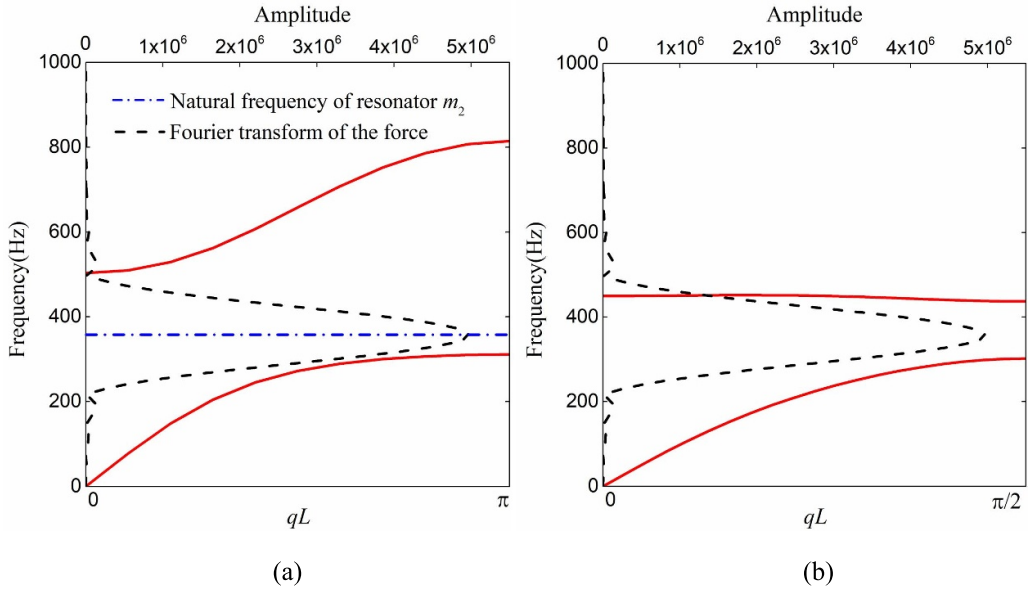

Figure 14. Dispersion relation curves of: (a) the classic local resonance system in figure 13(a); (b) the 2DOF SMT chain in figure 13(a). The Fourier transform of the force $F(t)$ is in the black dashed curve.

figure 13, a long and finite monatomic chain involving the proposed 2DOF SMT system and classic local resonance system in the middle is considered to monitor the wave space-time domain evolution and attenuation of the input signal. The classic local resonance system in figure 13(a) is set as a reference to evaluate the superiority of the proposed structure in broadband wave attenuation. It has been found that the intersection masses are meaningless for the bandgap generation, so there are no intersection masses in figure 13(b).

The left and right sides of the long finite chain in figure 13 are two monatomic chains of length 150, with masses $m_1 = 2$ Kg and springs $K_1 = 1\times10^7$ N m^{-1}. The middle of the long finite chain is a vibration absorption or attenuation device. Six unit cells of 1D periodic local resonant metamaterial are connected in the middle in figure 13(a) with $m_2 = 2$ Kg and $K_2 = 1\times10^7$ N m^{-1}. The middle vibration attenuation device is replaced by three unit cells of the 2DOF SMT chain in figure 13(b), and the total mass of the chain is fixed as that in figure 13(a) by assuming $m_{11} = 1$ Kg, $m_{12} = 3$ Kg with $G_1 = 4\times10^6$ N m^{-1}, $K_{1,2} = 1\times10^7$ N m^{-1} and $\alpha = \pi/8$.

An incident wavelet packet propagates to the right along the chain, which is generated by applying the force $F(t)$ to the leftmost mass, where

$$F(t) = \begin{cases} \dfrac{K_1}{2}\left(1-\cos\left(\dfrac{2\pi f_{\rm ct}t}{N_{\rm cy}}\right)\right)\cos\left(2\pi f_{\rm ct}t\right) & \text{for } t < \dfrac{N_{\rm cy}}{f_{\rm ct}} \\ 0 & \text{otherwise} \end{cases} \tag{21}$$

in which $N_{\rm cy}$ is the number of packet cycles and $f_{\rm ct}$ is the central wave frequency.

Figure 14 shows the dispersion curves for the two vibration attenuation systems and the Fourier transform of the force $F(t)$ with $N_{\rm cy} = 5$ and $f_{\rm ct} = \sqrt{K_2/m_2}/(2\pi) = 356$Hz. The central wave frequency $f_{\rm ct}$ is the frequency with the largest amplitude in wave packet spectrum analysis, which is selected as the natural frequency of the resonator m_2. For the classical local resonance system, vibration transmittance reaches the minimum at the natural frequency of the resonator [35]. As shown in figure 14(a), the bandgap of the classical local resonance system is roughly centered around the central wave frequency $f_{\rm ct}$ to make the wave packet transmission is as little as possible. In figure 14(b), the bandgap of the 2DOF SMT chain is also roughly centered around $f_{\rm ct}$.

Figure 15 illustrates the spatial evolution of the incident wave packet along the chains in figure 13. As shown in figures 15(a) and (c), the propagation of the incident packet coincides exactly in the monatomic chain before it spread to the classic local resonance system and SMT system at $t = 0.05$ s (yellow marked area). Meanwhile, the incident packet has interacted with the middle vibration attenuation device and been divided into a reflected component and a transmitted component at $t = 0.125$ s, as presented in figures 15(b) and (d). The shaded areas are the displacement ranges.

In figure 15(b), the majority energy of the incident packet is reflected by the classic local resonance system, and the maximum amplitude of the transmitted component (0.14) at $t = 0.125$ s in figure 15(b) is 16.7% of the incident wave packet (0.84) at $t = 0.05$ s in figure 15(a). The result in figure 15(d) is significant that only 3.8% of the wave packet transmits the chain containing the 2DOF SMT system (0.032), which is 22.8% of that through the classic local resonance system (0.14). Hence, the results are sufficient to demonstrate the superiority of the proposed structure in broadband wave attenuation.

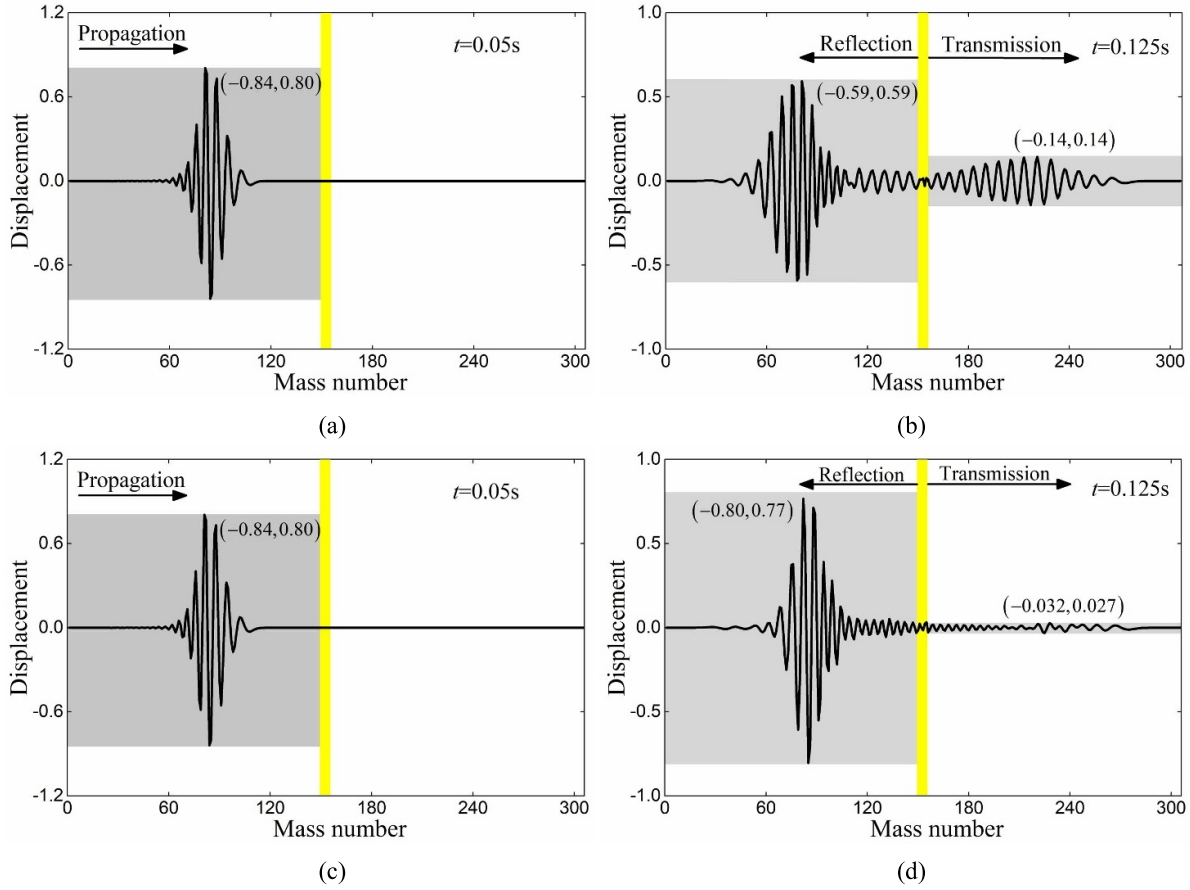

Figure 15. Spatial profile of the evolution of the incident wave packet along the chains containing: (a), (b) six unit cells classic local resonance system; (c), (d) three unit cells 2DOF SMT chain at $t = 0.05$ s (the left-hand panels) and $t = 0.125$ s (the right-hand panels). The location of the vibration attenuation structure is shaded in yellow.

4. Conclusion

In this paper, the bandgap characteristic and wave propagation behavior of a scissor-like elastic metamaterial are proposed for low-frequency vibration attenuation. Firstly, the 1DOF scissor-like SMT chain is studied, where the resonance and anti-resonance frequencies strictly correspond to the positive and negative peaks in transmission curves. The parameter condition for the lowest cut-off frequency is obtained based on the analytical expressions of dispersion curves.

Then, the 2DOF SMT chain is considered to generate an additional wide bandgap below the cut-off frequency of the 1DOF chain. The bandgap will be closed if the shear stiffness is too small, and the critical shear stiffness is suggested for bandgap generation based on the analytical expressions of bandgap boundaries. The dependence of bandgap on structure parameters can be summed up as that bigger difference between adjacent parameters or smaller angles are beneficial to widen and lower the bandgap. Meanwhile, the presence of intersection masses is meaningless for the bandgap generation.

Finally, the wave space evolution of an incident wave packet is conducted to illustrate the broadband wave attenuation properties of the proposed scissor-like system. Only 3.8% of the input wave packet transmits the proposed structure lattice with three units, which is 22.8% of that through the classic 1D local resonance metamaterial. The proposed scissor-like metamaterial shows a tunable bandgap and strong vibration attenuation of the broadband wave, based on the traditional scissor-like vibration isolation platform. Future work should focus on numerical simulations and the experiment of application-oriented structures.

Data availability statement

All data that support the findings of this study are included within the article (and any supplementary files).

Acknowledgments

The authors would like to acknowledge the financial support from the National Natural Science Foundation of China (12172383) and the Project of State Key Laboratory of High Performance Complex Manufacturing (ZZYJKT2020).

ORCID iDs

Yingli Li https://orcid.org/0000-0002-5843-2848
Xiang Liu https://orcid.org/0000-0002-4933-9756

References

[1] Xiao X, He Z C, Li E and Cheng A G 2019 Design multi-stopband laminate acoustic metamaterials for structural-acoustic coupled system *Mech. Syst. Signal Process.* **115** 418–33

[2] Fang X, Wen J, Yu D, Huang G and Yin J 2018 Wave propagation in a nonlinear acoustic metamaterial beam considering third harmonic generation *New J. Phys.* **20** 123028

[3] Cavalieri T, Cebrecos A, Groby J P, Chaufour C and Romero-García V 2019 Three-dimensional multiresonant lossy sonic crystal for broadband acoustic attenuation: application to train noise reduction *Appl. Acoust.* **146** 1–8

[4] Lei S, Ge Y and Li Q 2020 Effect and its mechanism of spatial coherence of track irregularity on dynamic responses of railway vehicles *Mech. Syst. Signal Process.* **145** 106957

[5] Jung J, Kim H G, Goo S, Chang K J and Wang S 2019 Realisation of a locally resonant metamaterial on the automobile panel structure to reduce noise radiation *Mech. Syst. Signal Process.* **122** 206–31

[6] Sun X and Jing X 2016 Analysis and design of a nonlinear stiffness and damping system with a scissor-like structure *Mech. Syst. Signal Process.* **66–67** 723–42

[7] Jing X, Zhang L, Feng X, Sun B and Li Q 2019 A novel bio-inspired anti-vibration structure for operating hand-held jackhammers *Mech. Syst. Signal Process.* **118** 317–39

[8] Wu Z, Jing X, Bian J, Li F and Allen R 2015 Vibration isolation by exploring bio-inspired structural nonlinearity *Bioinspir. Biomim.* **10** 056015

[9] Wei C, Zhang K, Hu C, Wang Y, Taghavifar H and Jing X 2018 A tunable nonlinear vibrational energy harvesting system with scissor-like structure *Mech. Syst. Signal Process.* **125** 202–14

[10] Sridhar A, Liu L, Kouznetsova V G and Geers M G D 2018 Homogenized enriched continuum analysis of acoustic metamaterials with negative stiffness and double negative effects *J. Mech. Phys. Solids* **119** 104–17

[11] Wang K, Zhou J, Wang Q, Ouyang H and Xu D 2019 Low-frequency band gaps in a metamaterial rod by negative-stiffness mechanisms: design and experimental validation *Appl. Phys. Lett.* **114** 251902

[12] Huang H H, Sun C T and Huang G L 2009 On the negative effective mass density in acoustic metamaterials *Int. J. Eng. Sci.* **47** 610–7

[13] Chen M, Xu W, Liu Y, Yan K, Jiang H and Wang Y 2018 Band gap and double-negative properties of a star-structured sonic metamaterial *Appl. Acoust.* **139** 235–42

[14] Yao S, Zhou X and Hu G 2008 Experimental study on negative effective mass in a 1D mass–spring system *New J. Phys.* **10** 043020

[15] Liu Z, Zhang X, Mao Y, Zhu Y Y, Yang Z, Chan C T and Sheng P 2000 Locally resonant sonic materials *Science* **289** 1734–6

[16] Meaud J 2018 Multistable two-dimensional spring-mass lattices with tunable band gaps and wave directionality *J. Sound Vib.* **434** 44–62

[17] Yasuda H, Chong C, Charalampidis E G, Kevrekidis P G and Yang J 2015 Formation of rarefaction waves in origami-based metamaterials *Phys. Rev.* E **93** 043004

[18] Schenk M, Guest S D and Mcshane G J 2014 Novel stacked folded cores for blast-resistant sandwich beams *Int. J. Solids Struct.* **51** 4196–214

[19] Xu Z-L, Xu S-F and Chuang K-C 2021 Coupled flexural-longitudinal waves in an origami metamaterial with uncoupled creases *Phys. Lett.* A **396** 127232

[20] Yilmaz C and Hulbert G M 2010 Theory of phononic gaps induced by inertial amplification in finite structures *Phys. Lett.* A **374** 3576–84

[21] Yuksel O and Yilmaz C 2020 Realization of an ultrawide stop band in a 2D elastic metamaterial with topologically optimized inertial amplification mechanisms *Int. J. Solids Struct.* **203** 138–50

[22] Frandsen N M M, Bilal O R, Jensen J S and Hussein M I 2016 Inertial amplification of continuous structures: large band gaps from small masses *J. Appl. Phys.* **119** 124902

[23] Yilmaz C, Hulbert G M and Kikuchi N 2007 Phononic band gaps induced by inertial amplification in periodic media *Phys. Rev.* B **76** 54309

[24] Bennetts L G, Peter M A, Dylejko P and Skvortsov A 2019 Effective properties of acoustic metamaterial chains with low-frequency bandgaps controlled by the geometry of lightweight mass-link attachments *J. Sound Vib.* **456** 1–12

[25] Matlack K H, Serra-Garcia M, Palermo A, Huber S D and Daraio C 2018 Designing perturbative metamaterials from discrete models *Nat. Mater.* **17** 323–8

[26] Chen Y Y, Barnhart M V, Chen J K, Hu G K, Sun C T and Huang G L 2016 Dissipative elastic metamaterials for broadband wave mitigation at subwavelength scale *Compos. Struct.* **136** 358–71

[27] Chang I L, Liang Z-X, Kao H-W, Chang S-H and Yang C-Y 2018 The wave attenuation mechanism of the periodic local resonant metamaterial *J. Sound Vib.* **412** 349–59

[28] Huang H H and Sun C T 2011 Theoretical investigation of the behavior of an acoustic metamaterial with extreme Young's stiffness *J. Mech. Phys. Solids* **59** 2070–81

[29] Bobrovnitskii Y I 2014 An acoustic metamaterial with unusual wave properties *Acoust. Phys.* **60** 371–8

[30] Huang H H and Sun C T 2012 Anomalous wave propagation in a one-dimensional acoustic metamaterial having simultaneously negative mass density and Young's stiffness *J. Acoust. Soc. Am.* **132** 2887–95

[31] Kushwaha M S, Djafari-Rouhani B and Dobrzynski L 1998 Sound isolation from cubic arrays of air bubbles in water *Phys. Lett.* A **248** 252–6

[32] Bartlett F D and Flannelly W G 1974 Application of antiresonance theory to helicopters *J. Am. Helicopter Soc.* **19** 11–15

[33] Zhou W J, Li X P, Wang Y S, Chen W Q and Huang G L 2018 Spectro-spatial analysis of wave packet propagation in nonlinear acoustic metamaterials *J. Sound Vib.* **413** 250–69

[34] Devaux T, Tournat V, Richoux O and Pagneux V 2015 Asymmetric acoustic propagation of wave packets via the self-demodulation effect *Phys. Rev. Lett.* **115** 234301

[35] Hussein M I, Leamy M J and Ruzzene M 2014 Dynamics of phononic materials and structures: historical origins, recent progress, and future outlook *Appl. Mech. Rev.* **66** 040802